Secondary Project Proposal

Post-seismic deformation of Chi-chi earthquake

Yunyue (Elita) Li

11:00, Wednesday, June 2, 2010

MOTIVATION

Personal prospective

My interests for earthquake deformation were initially motivated by the 2008 Wenchuan, China earthquake. Casualties during this magnitude 8.0 earthquake were shown by the government as follows: dead 69,142; missing 17,921; injured 374, 065. This earthquake was felt strongly by the whole nation, both physically and mentally. While people all over the country and the world were offering their help to Wenchuan, I questioned myself: as a geophysicist, what you can do to render help? In addition to claiming that earthquake is not predictable, can I provide at least some understanding of the earthquake?

Research prospective

Postseismic deformation is widely observed following large earthquakes. Study of postseismic deformation is essential to the understanding of the physics of the earthquake nucleation as a time-dependent process. Also, postseismic deformation redistributes the stress in the crust and thus influences the occurrence of future earthquakes.

Segall (2010) points out that postseismic deformation could be explained by many mechanical processes, including viscous relaxation of rock below the seismogenic zone; transient fault slip (afterslip), either within the rupture zone or below the rupture zone; and flow of pore fluids induced by the earthquake. While the poroelastic effects on the observable crustal deformation have only been recently recognized, differentiating the effects of viscoelastic relaxation and afterslip have been an active area of research for a long time (Thatcher, 1983; Barker, 1976; Hsu et al., 2007).

Thatcher (1983) studied afterslip and viscoelastic relaxation effects using *thick lithosphere* and *thin lithosphere* model, respectively. He concluded in that paper that contributions of afterslip and viscoelastic relaxation couldn't be differentiated based on the fitting on the data from California. Segall (2010) also showed the mathematical equivalence between these two models for the infinitely long strike-slip faults. However, for finite, dip-slip faults, there is still a chance to differentiate the effects of these two different mechanisms.

In the early studies of the 1999 Chi-Chi Taiwan earthquake, Yu et al. (2003); Hsu et al. (2007) and Hsu et al. (2002) conclude that afterslip is the dominant mechanism of post-seismic deformation in the 15-month period following the Chi-Chi earthquake. However, Sheu and Shieh (2004) claim a concurrence of afterslip and viscoelastic relaxation, with afterslip dominated the near field post-seismic deformation, and viscoelastic relaxation dominated the far field. After 10 years of Chi-Chi earthquake, a large amount of continuous and Campaign GPS data are obtained. Therefore, another analysis is necessary to determine the contribution of different mechanisms in

a relatively longer period.

INTRODUCTION

On September 21, 1999, Chi-Chi Taiwan earthquake struck central Taiwan, and caused a 100-km-long surface rupture. Thanks to the extensive network of sensors and monitoring stations, this quake is one of the best recorded large quakes in history, and thereby of significant research value.

This magnitude 7.6 earthquake was caused by the rupture of the Chelungpu fault (CLPF), the main part of which is a north-south-striking trust fault that dips about 30-degree to the east. It is part of the western thrust zone that accommodates some of the crustal shortening caused by the collision of the Philippine Sea and the Eurasia Plate. The surface rupture has a sharp turn to the east at the north end of the CLPF, where the maximum horizontal and vertical surface displacements of up to 8-10m were recorded (Lee et al., 2002). Coseismic GPS displacements show much larger vertical and horizontal movements on the hanging wall than that on the footwall (Yu, 2001).

The inversions of geodetic and seismic data for the coseismic slip distribution all yield similar results: a maximum slip of about 10-15m localized at the northern end of the fault, and extending about 10km downdip from the ground surface (Ji et al., 2001; Johnson et al., 2001; Ma et al., 2001; Zeng and Chen, 2001; Loevenbruck et al., 2004). On the contrary, only a small net slip – about 1-2m – was observed at the southern end of the fault near the epicenter.

Previous studies of the post-seismic GPS displacements have different understanding for the role of afterslip and viscoelastic relaxation. Hsu et al. (2007) evaluated the contributions of afterslip and viscoelastic relaxation of the lower crust and upper mantle using GPS displacement data collected in the 15 months after the 1999 Chi-Chi earthquake (M_ω7.6). By seeing a much better fit using the afterslip models than viscoelastic models, they concluded that afterslip is the dominant mechanism in the first 15-month period. On the other hand, Sheu and Shieh (2004) analyze the GPS displacement in the 97-day period after the Chi-Chi main shock and conclude that afterslip dominated the near field post-seismic deformation, while viscoelastic relaxation dominated the far field.

In this project, I will analyze the effects of afterslip and viscoelastic relaxation of the lower crust and upper mantle with the GPS recorded displacement in the 10-year period after the main shock. In a relatively long term, the dominant mechanism for the post-seismic deformation may change. By analyzing the temporal and spatial evolution of the post-seismic deformation, I hope to differentiate the contributions from these two mechanisms.

THEORY

Viscoelastic relaxation

From the first chapter of Segall (2010) quasi-static deformational surface displacements can be obtained by solving the following set of governing equations: kinematic equations:

$$\epsilon_{ij} \equiv \frac{1}{2}(\frac{\partial u_i}{\partial x_j} + \frac{\partial u_j}{\partial x_i}), \tag{1}$$

quasi-static equilibrium equations:

$$\frac{\partial \sigma_{ij}}{\partial x_j} + \rho f_i = 0, \tag{2}$$

and constitutive laws (they vary from one material to another, I am writing here the one for linear elastic material):

$$\sigma_{ij} = C_{ijkl}\epsilon_{kl}, \tag{3}$$

where u_i is the displacement in the i_{th} direction, ϵ_{ij} is the strain tensor, σ_{ij} is the stress tensor, f_i is the body force, ρ is the density, C_{ijkl} is the symmetric fourth-rank stiffness tensor, and $i, j = 1, 2, 3$. This is a closed system with 15 equations (6 kinematic equations, 3 equilibrium equations and 6 constitutive equations), and 15 unknowns (3 displacements, 6 stresses and 6 strains). When dealing with different cases of surface deformation, we are actually solving this set of equations using different boundary conditions in space and initial conditions in time.

Compared with the elastic problems, the equilibrium equations and the kinematic equations remain the same, while the constitutive laws are different for the viscoelastic case. Visoelastic models can be in general thought of as combinations of elastic and viscous elements. Figure 1 shows the well-known Maxwell material where a elastic element, represented by a spring, and a viscous element, represented by a dashpot, are chained in series. To formulate the constitutive laws, notice that the total strain rate is the sum of the strain rate in the spring and the dashpot. At the same time, force balance requires that the stress must be the same in each element; therefore:

$$\begin{aligned} \dot{\epsilon}_{total} &= \dot{\epsilon}_{spring} + \dot{\epsilon}_{dashpot} \\ &= \frac{\dot{\sigma}}{2\mu} + \frac{\sigma}{2\eta} \end{aligned} \tag{4}$$

where the superimposed dot amounts to the time derivative, μ is the elasticity of the spring, and η is the viscosity of the dashpot.

Understanding of the behavior of the Maxwell material can be obtained by analyzing equation (4). For a step change in stress σ_0, the material first deforms elastically by an amount of $\sigma_0/2\mu$, because the dashpot has no time to relax yet. Afterward, the material strains at a constant rate of $\sigma_0/2\eta$. Therefore, the material behaves elastically at short time, but viscously at long times. On the other hand, if the system has a sudden strain change ϵ_0, which is held constant thereafter, the stress will

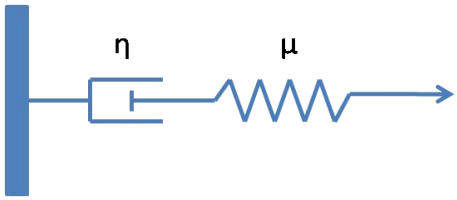

Figure 1: Maxwell material model for viscoelastic media.

instantaneously rise by an amount of $2\mu\epsilon_0$. After that, the total is strain is constant, so the stress evolution with time can be obtained by solving the differential equation (4) with zero on the left-hand side. The result is the so-called *relaxation function*:

$$\sigma = 2\mu\epsilon_0 e^{-\frac{\mu}{\eta}t} \qquad t > 0, \tag{5}$$

demonstrating that the Maxwell material has a characteristic relaxation time of $t_r = \eta/\mu$.

According to the *correspondence principle* (Segall, 2010), the visocoelastic problem can be solved as an elastic problem in the *Laplace transform* domain. The corresponding elastic parameters are given as follows:

$$\bar{\mu} = \frac{s\mu}{s + \frac{\mu}{\eta}}, \tag{6}$$

and

$$\bar{\lambda} = \frac{s\lambda + K\frac{\mu}{\eta}}{s + \frac{\mu}{\eta}}, \tag{7}$$

where s is the Laplace transform variable, μ and η are the elasticity and viscosity in the physical domain, $\bar{\mu}$ and $\bar{\lambda}$ are the corresponding elastic parameters in the Laplace domain. Hereafter, all the method derived for the elastic media can be applied to the corresponding elastic media, solution of which can be inverse transformed and then used as the solution to the viscoelastic problem.

Afterslip

The study of afterslip is a part of the study of fault friction, which leads to the discussion of the earthquake nucleation. Current understanding of the fault friction mechanism is based on the *spring-slider* model, as shown in Figure 2. The block is pressed against a flat interface with normal stress σ. The spring has stiffness k and is driven at the plate velocity v_{plate}. The cumulative displacement of the block is δ and the friction resistance to slip is τ.

Following the rate-and-state friction theory, the governing equations for the spring-slider system are:

$$\dot{v} = (\frac{\eta}{\sigma} + \frac{a}{v})^{-1}(\frac{\dot{\tau}}{\sigma} - \frac{b\dot{\theta}}{\theta}), \tag{8}$$

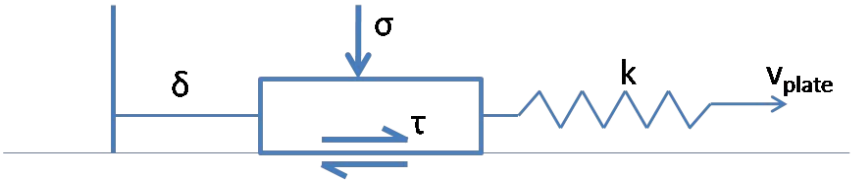

Figure 2: Single freedom spring-slider model for the rate and state fault friction.

$$\dot{\theta} = 1 - \frac{\theta v}{d_c} \quad or \quad \dot{\theta} = -\frac{v\theta}{d_c} ln(\frac{v\theta}{d_c}), \tag{9}$$

and

$$\dot{\tau} = k(v^{\infty} - v), \tag{10}$$

where $\eta = \mu/2v_s$, μ is the shear modulus, and v_s is the shear wave velocity (Rice, 1983); θ is the scaler state variable; d_c is the characteristic displacement scale; a and b are the weighting coefficients for the rate and state component, respectively; and v^{∞} is the block velocity at equilibrium. The first and second evolution equation in Equation (9) are referred as the *aging law* and the *slip law*, respectively.

After the main shock of the earthquake, coseismic rupture must decelerate from seismic slip rate. Numeriacal simulations of the system above show that the fault tends to decelerate at approximately constant stress (Segall, 2010). Theoretically, afterslip can be triggered with either velocity-strengthening or velocity-weakening friction. However, according to the numerical analysis and the lab observations, the cases for stable transients with velocity-weakening friction are limited (Segall, 2010). Therefore, I will focus on afterslip in velocity-strengthening regions surrounding the coseismic rupture zone. Since the velocity-strengthening regions, that are the afterslip zones, are usually large compared with the nucleation dimensions, it is likely that the stiffness of the afterslip zone is sufficiently low and the system tends to decelerate along the steady-state line. With all these assumptions, the governing equation for steady-state frictional afterslip is:

$$\sigma(a-b)\frac{\dot{v}}{v} = k(v^{\infty} - v), \tag{11}$$

with the initial condition:

$$v(t=0) = v_{max} = v^{\infty} exp[\Delta\tau/(a-b)\sigma]. \tag{12}$$

Solving the system of equation (11) and (12), the afterslip and slip rate are given as follows:

$$\delta(t) = \frac{\sigma(a-b)}{k} ln\big(\frac{e^{t/t_c} - C}{1-C}\big), \tag{13}$$

$$v(t) = \frac{v^{\infty}}{1 - Ce^{-t/t_c}}, \tag{14}$$

where

$$C = \frac{v_{max} - v^{\infty}}{v_{max}}, \tag{15}$$

$$t_c = \frac{\sigma(a-b)}{kv^{\infty}}. \tag{16}$$

Notice the characteristic decay time depends both on the frictional properties and the on the stiffness of the system. The more compliant (larger) the afterslip zones, the longer transients they will experience. At short times $t \ll t_c$, equation (13) can be approximate by the summation of a linear part and a logarithm part as follows:

$$\tilde{\delta}(t) = \frac{\sigma(a-b)}{k} ln\big[\frac{kv_{max}}{\sigma(a-b)}t + 1\big] + v^{\infty}t. \tag{17}$$

For a fault in an elastic medium, the size of the aseismically slipping region is not known as a prior and will generally change with time. Then, the constant stiffness assumption implied by the spring-slider model won't be valid. Therefore, caution is needed when applying the single freedom spring-slider model on faults in nature.

WORK COMPLETED

Data fitting

I got the GPS time series data in the 10-year period after 1999 Chi-Chi earthquake from Ya-Ju Hsu, Institute of Earth Sciences, Academia Sinica, Taiwan. There are data from 31 continuous GPS stations and 87 campaign GPS stations, given in the format of name, longitude, latitude, height, recording time, northern displacement, eastern displacement and uplift at each station. No uncertainties are included in the data, and the preseismic velocities (secular motion) are not corrected. In this project, I am looking at the eastern displacement in particular, which approximately points perpendicular to the fault.

I fit the eastern displaecement data by the parametric function as follows:

$$\delta = \delta_0 + Aln(1 + \frac{t}{t_c}) + v^{\infty}t, \tag{18}$$

which is similar to the displacement given by equation (17). In equation (18), δ and t are the input, obtained from the GPS measurements; δ_0, A, t_c and v^{∞} are the parameters that are going to be estimated from the data.

Figure 3 and 4 show the comparison between the observed eastern displacements with the fitted curve for selective continuous and campaign GPS stations, respectively. As shown in the figures, time series from some stations are well fitted, while others are not. Continuous station 1 and 11 show a strong evidence for the transient displacements, same as campaign station 4, 7, 9, and 10.

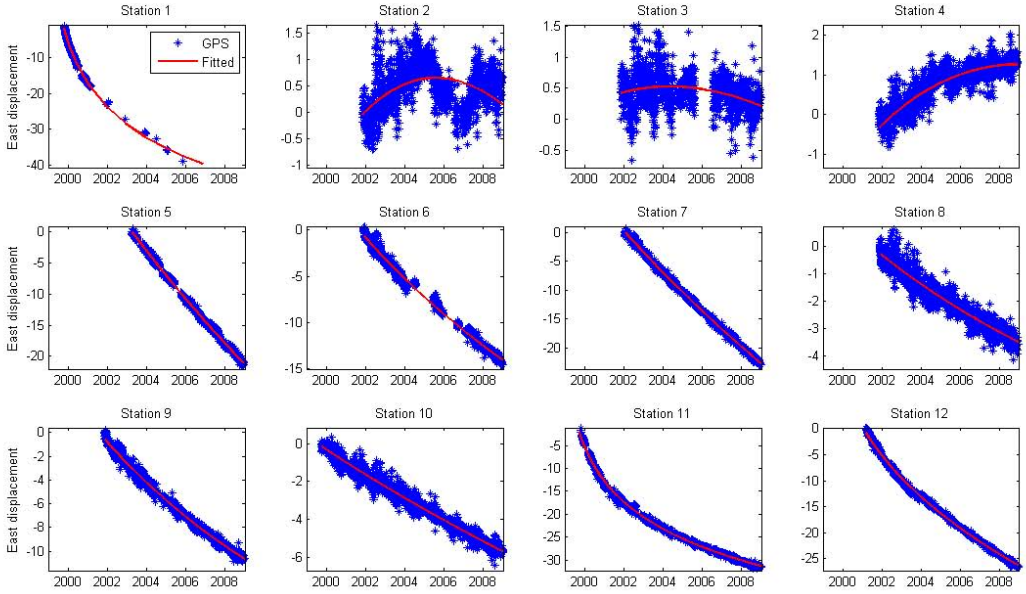

Figure 3: Comparison between observed GPS displacements and the fitted curve for selective continuous GPS stations.

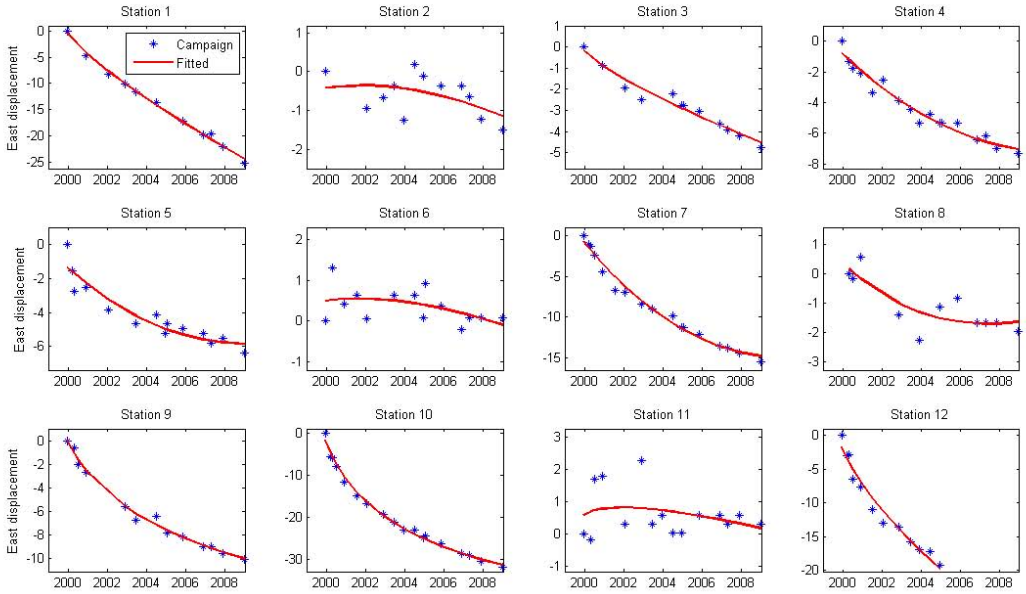

Figure 4: Comparison between observed GPS displacements and the fitted curve for selective campaign GPS stations.

I filter out the stations with large apparent noise, such as campaign GPS station 6 in figure 4, and compute the velocity at each year with the fitted data. The selected stations are scattered in figure 6, where the red star denotes the projection of the epicenter on the fault. The longitude and latitude of each station is tranformed to the local coordinate with respect to the red start. After filtering, only 13 continuous and 18 campaign GPS stations are left for analysis. It is obvious that the selected campaign GPS stations are very close to the fault.

The stations are projected to the profile perpendicular to the CLPF to compare with the 2-D modeled result, and velocity with respect to the distance from the fault is plotted in figure 5. The top panel shows the velocity from the continuous GPS stations, while the bottom panel shows that from the campaign stations. The vertical bar at zero denotes the position where CLPF comes to the surface. Clearly, the velocity is decreasing with time, and pointing to the west.

Visoelastic modeling

The viscoelastic modeling code calculates the displacements at time t due to uniform slip on a dislocation in an elastic layer overlaying a Maxwell viscoelastic half-space. The 2-D model gird extends horizontally 100km east and 60km west off the CLPF, as shown in figure 7. The vertical domain has a 20km elastic layer and a Maxwell viscoelastic half-space. The simplified input for the coseismic fault geometry and slip distribution of Chi-Chi earthquake is based on the results given by Yu et al. (2003). The east-dipping CLPF has an average of 4m slip during the coseismic deformation, which extends 12km downdip.

Figure 8 and 9 show the cumulative displacements and the velocity given by the viscoelastic modeling, respectively. The vertical bar at zero denotes the fault trace at the surface. The panel on top in each figure show the spatial variation of the displacements and velocity at three different times, while the bottom panel show the temporal variation at two different locations. Obviously, the displacement and velocity at a fix location show nearly linear relationship with respect to time.

Compared figure 9 with figure 5, the viscoelastic model predicts a positive slip rate near the fault on the hanging wall, while the observed data show the opposite sign. However, at the far field, the modeled data show the similar trend as the observed data. This may provide a hint that viscoelastic model is the dominant mechanism at the far field, similar to the conclusion of Sheu and Shieh (2004).

Afterslip modeling

The modeling for the afterslip is still preliminary. The current code calculates the post-seismic deformation at time t due to the afterslip on an antiplane strike-slip fault (Figure 10). As a 2-D model as well, it is further off to the real case than the

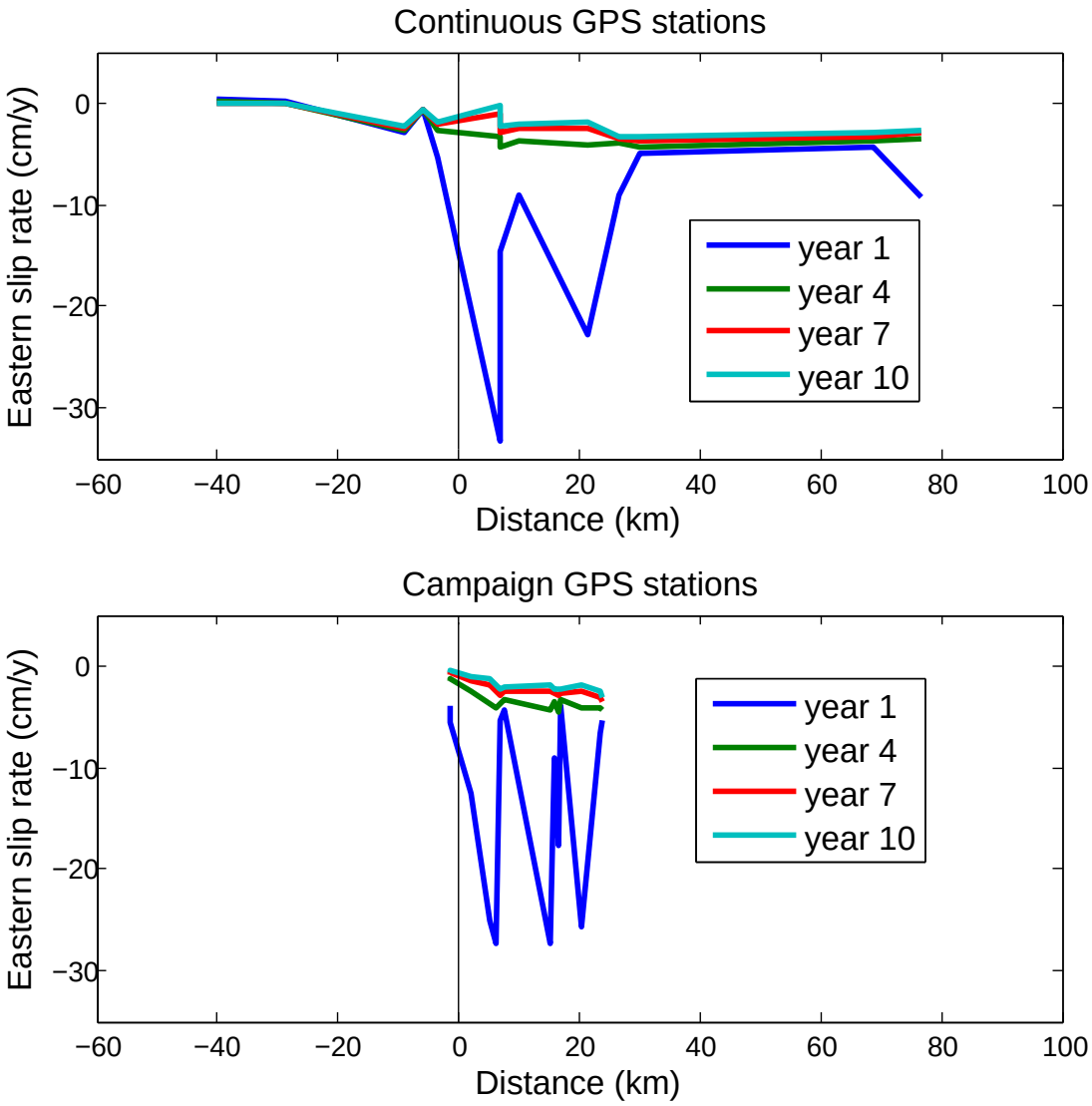

Figure 5: Observed velocity from the continuous GPS stations and campaign GPS stations.

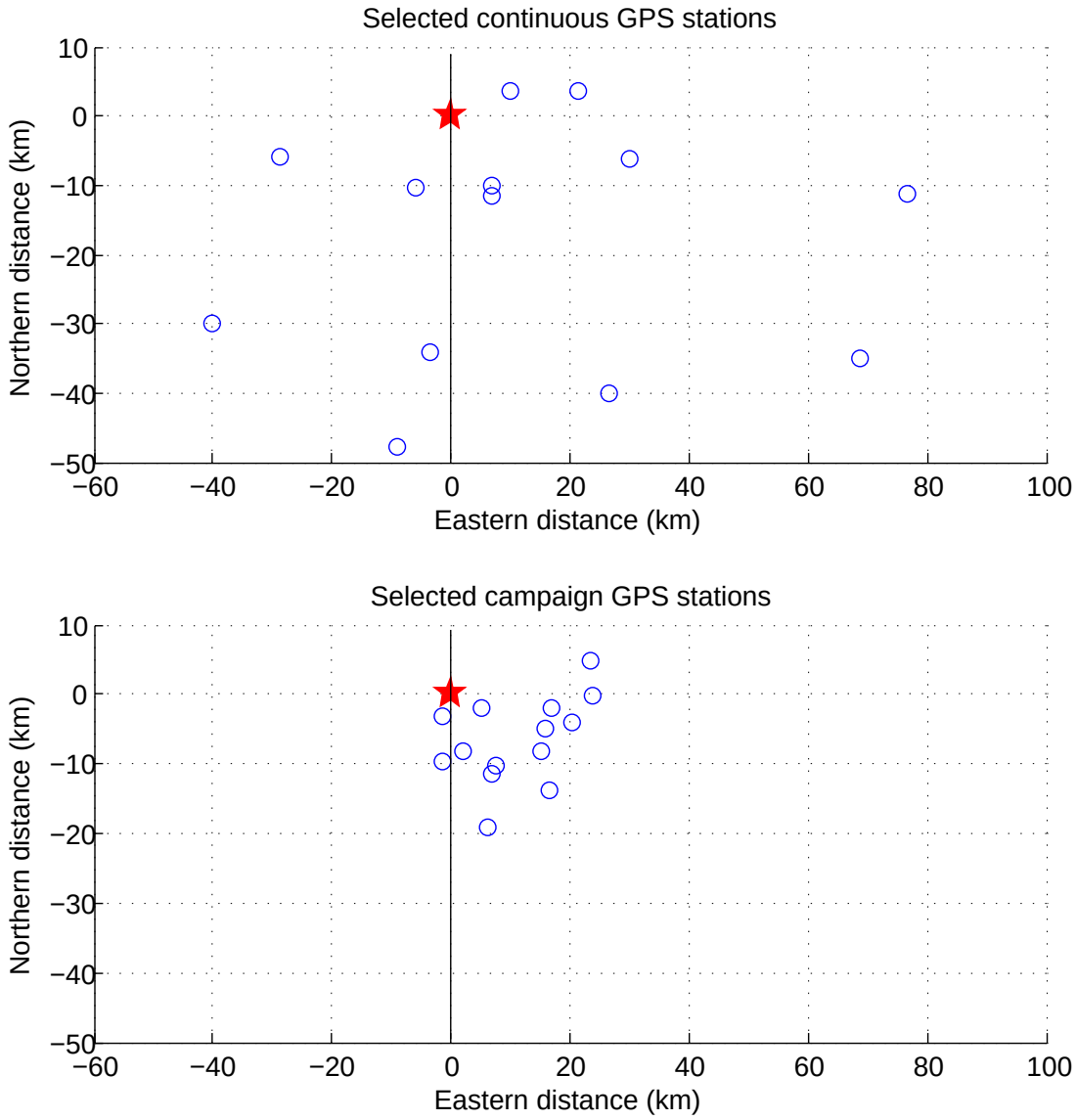

Figure 6: Map view of selected continuous and campaign GPS stations.

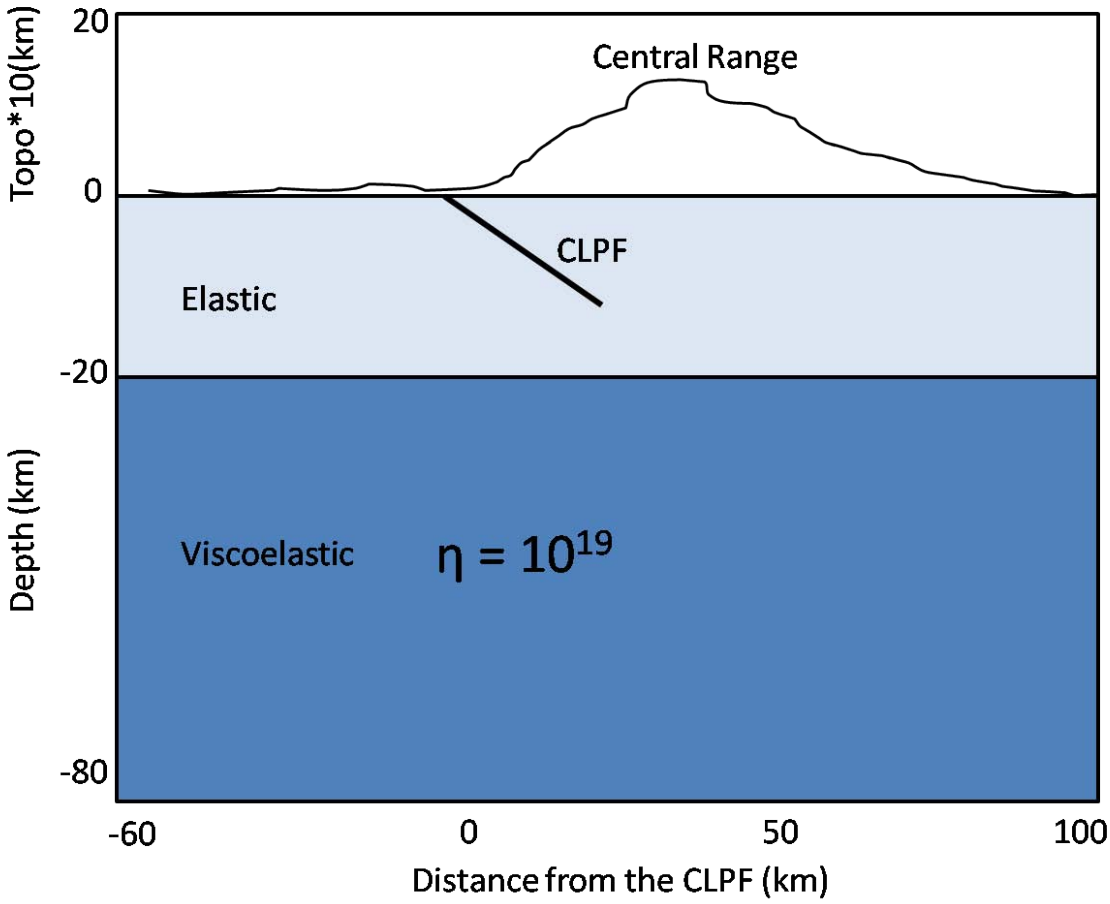

Figure 7: The viscoelastic model consisting of an elastic layer and a viscoelastic half-space.

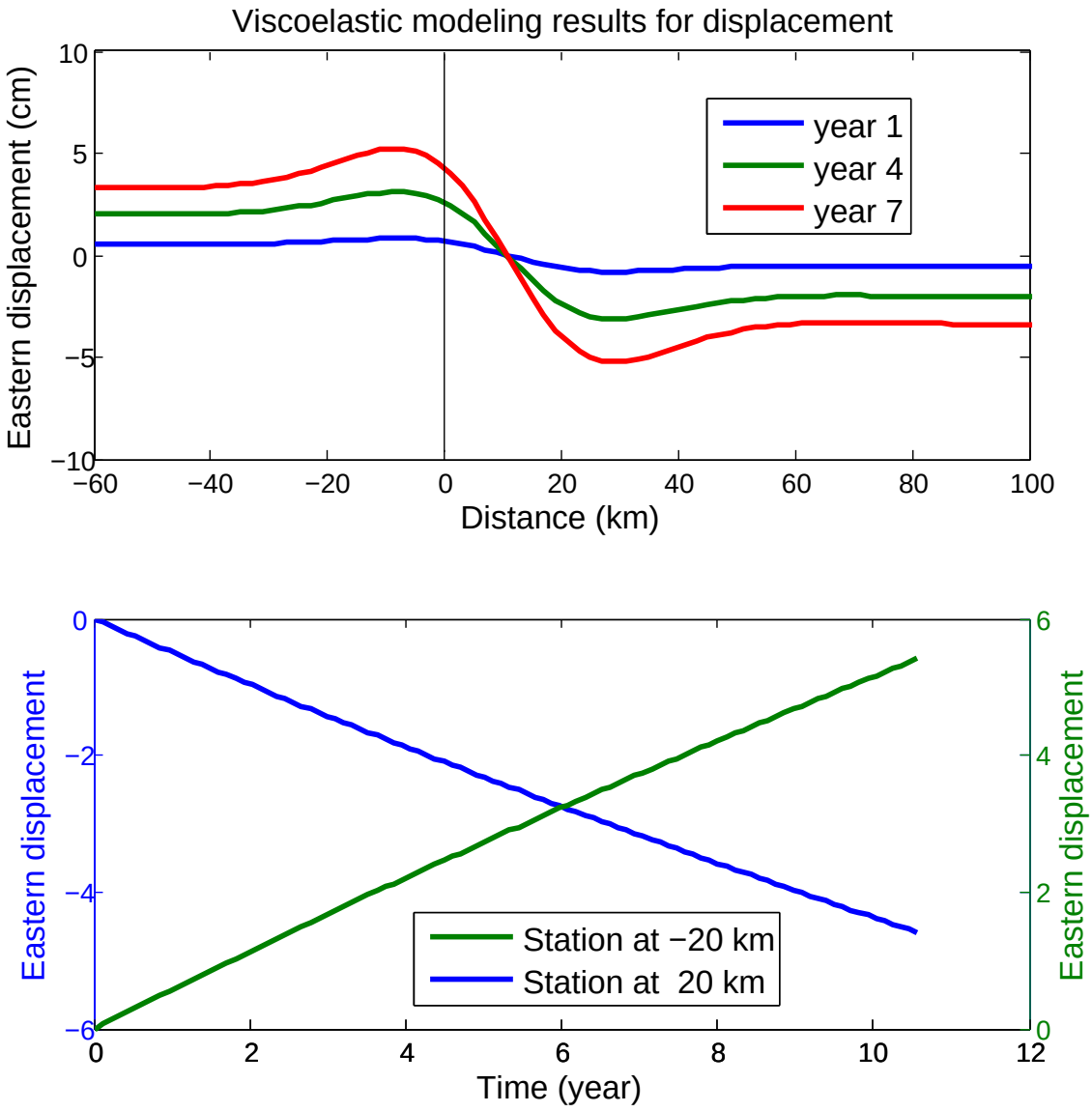

Figure 8: Displacements modeled by viscoelastic model. The panel on top shows the spatial variation of the displacement at fix times, and the panel on the bottom shows the temporal variation of the displacement at fix locations. Notice the linear trend at each station.

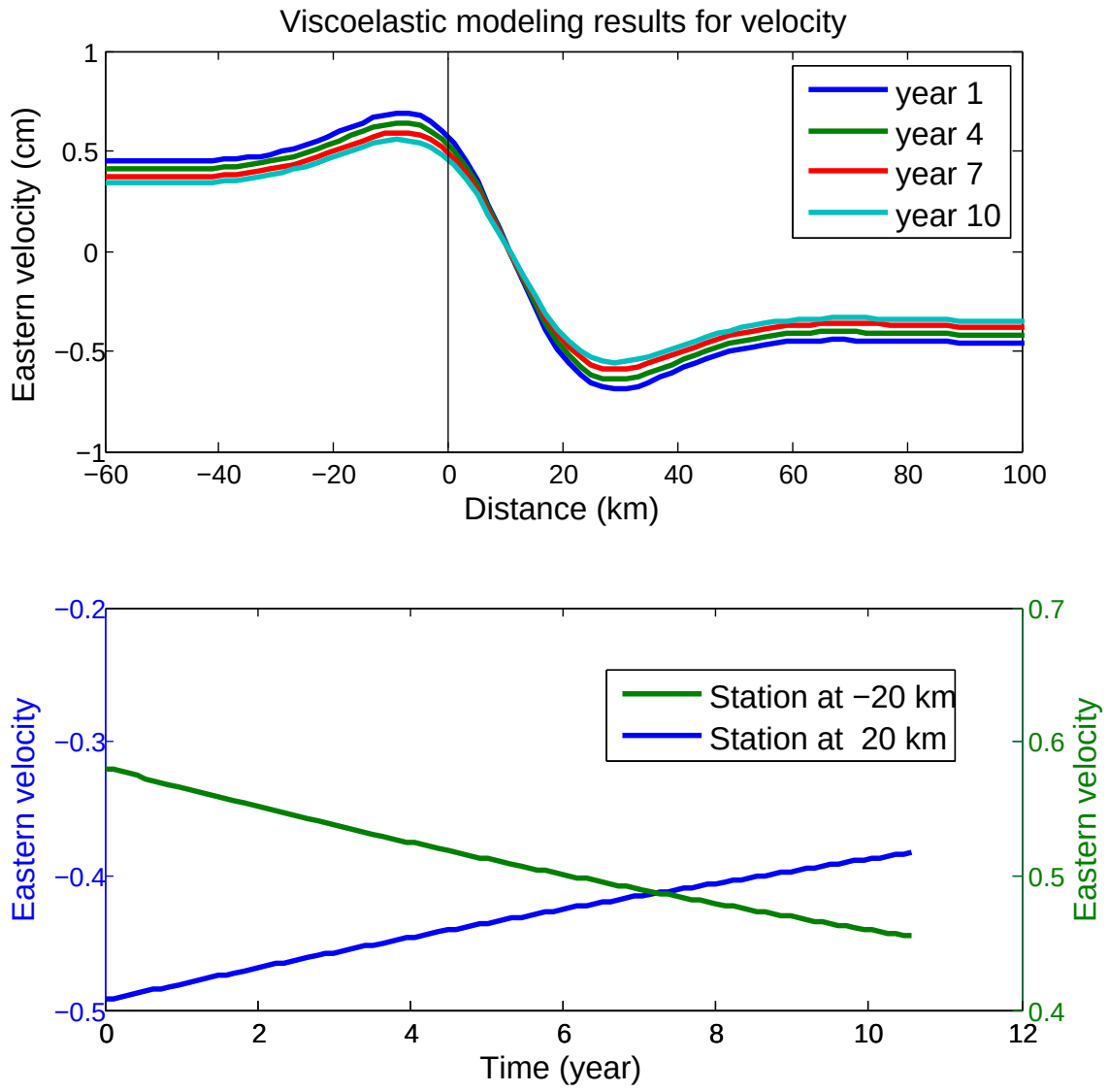

Figure 9: Velocity modeled by viscoelastic model. The panel on top shows the spatial variation of the velocity at fix times, and the panel on the bottom shows the temporal variation of the velocity at fix locations. Notice the linear trend at each station.

viscoelastic model.

Figure 11 and 12 show the displacements and the velocity modeled by the simply afterslip model. The vertical bar at zero denotes the fault trace at the surface. The panel on top in each figure show the spatial variation of the displacements and velocity at three different times, while the bottom panel show the temporal variation at two different locations.

It is difficult to make sensible comparisons because of the over-simplified model. However, notice the logarithmic charactor in the temporal variation at a fix location, which also shows up in the data at various locations. This may also give a hint that at certain stations, the afterslip effect is dominant.

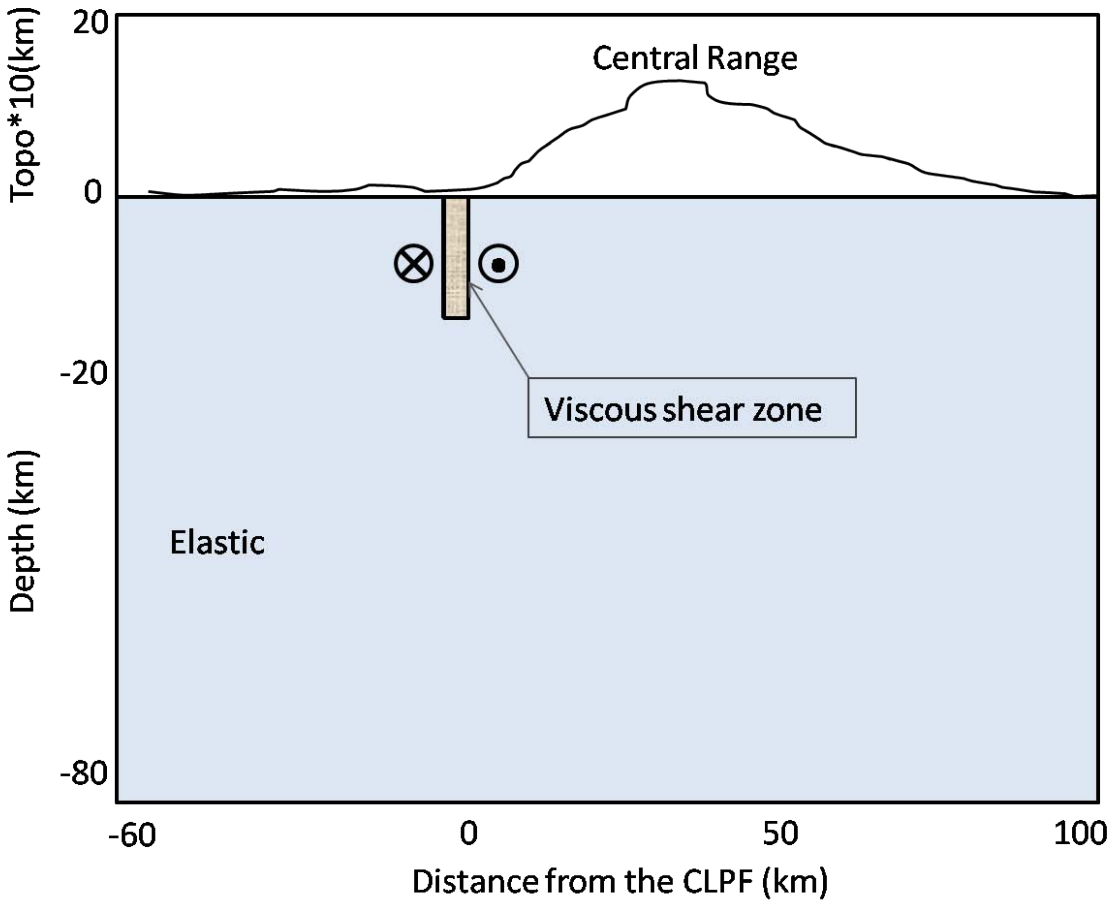

Figure 10: Antiplane strike-slip afterslip model with a viscous shear zone.

FUTURE WORK

There are several topics that I would like to work on in the future.

Better handling with the data. As can be seen from figure 5, the slip rate that I

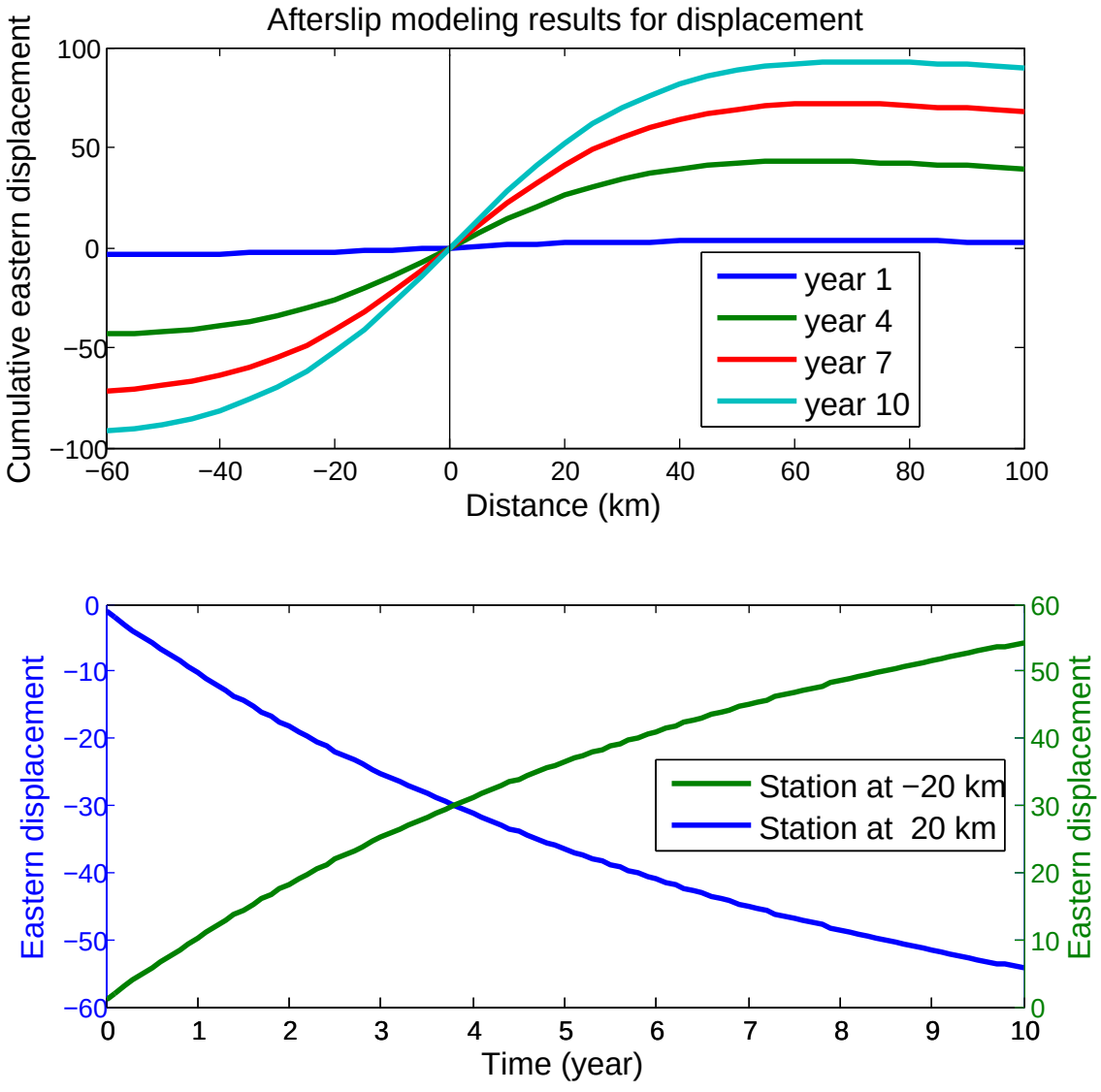

Figure 11: Displacements modeled by afterslip model. The panel on top shows the spatial variation of the displacement at fix times, and the panel on the bottom shows the temporal variation of the displacement at fix locations. Notice the logarithmic trend at each station.

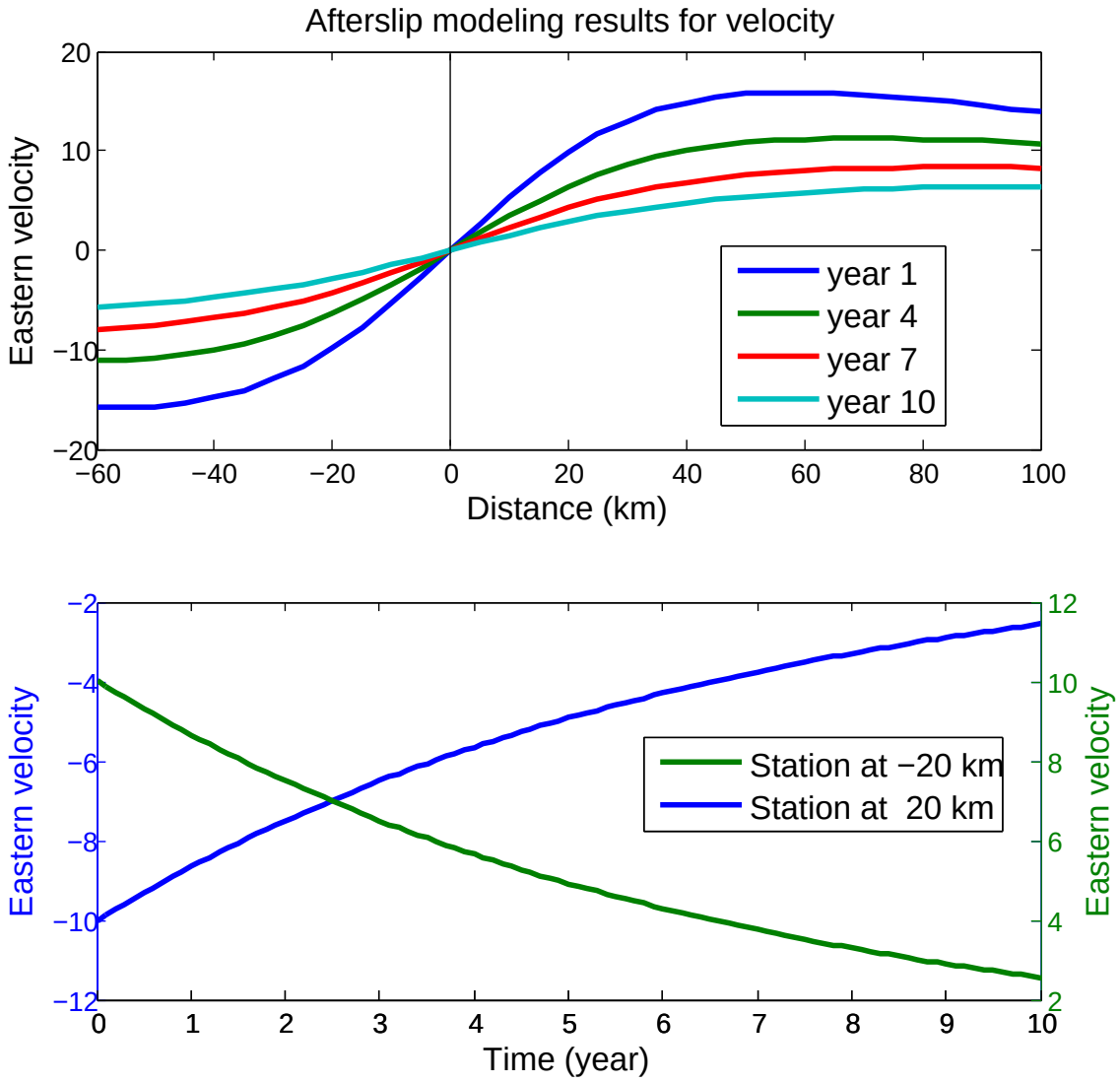

Figure 12: Velocity modeled by afterslip model. The panel on top shows the spatial variation of the velocity at fix times, and the panel on the bottom shows the temporal variation of the velocity at fix locations. Notice the logarithmic trend at each station.

get from the data is very noisy. Also, the preseismic velocities are not corrected from the data. Therefore, more efforts should be devoted to better handle the data and get a cleaner slip rate trend.

More realistic afterslip models. Current afterslip model cannot provide a sensible comparison between the modeled data and the observed data. As a first step to improve, I can compute the displacement due to full relaxation of the coseismic stress changes using a BEM approach. Later on, I may get code from Kaj Johnson which can compute the displacement with more realistic models.

Test the combination of these two models. The data given by viscoelastic modeling have large misfits near the fault, but the similar trend away from the fault. Also, the over-simplified afterslip model yields similar logarithmic displacement trend at various stations. Therefore, a certain combination of these two models might be a better explanation of the surface deformation.

I hope to work on the topics above in the summer, and produce a integrated paper before the deadline of AGU fall meeting in 2010.

REFERENCES

Barker, T., 1976, Quasi-static motions near the San Andreas fault zone: Geophysical Journal of the Royal Society, **45**, 689–705.

Hsu, Y., P. Segall, S.-B. Yu, L.-C. Kuo, and C. A. Williams, 2007, Temporal and spatial variations of post-seismic deformation following the 1999 Chi-Chi, Taiwan earthquake: Geophys. J. Int., **169**, 367–379.

Hsu, Y.-J., N. Bechor, P. Segall, S.-B. Yu, and L.-C. Kuo, 2002, Rapid afterslip following the 1999 Chi-Chi, Taiwan earthquake: GEOPHYSICAL RESEARCH LETTERS, **29**, 10.1029/2002GL014967.

Ji, C., D. Helmberger, T. Song, K. Ma, and D. Wald, 2001, Slip distribution and tectonic implication of the 1999 Chi-Chi, Taiwan, earthquake: Geophys. Res. Lett., **28**, 4379–4382.

Johnson, K., Y. Hsu, P. Segall, and S. Yu, 2001, Fault geometry and slip distribution of the 1999 Chi-Chi Taiwan earthquake imaged from inversion of gps data: Geophys. Res. Lett., **28**, 2285–2288.

Lee, J., H. Chu, J. Angelier, Y. Chan, J. Hu, C. Lu, and R. Rau, 2002, Geometry and structure of northern surface ruptures of the 1999 mw=7.6 Chi-Chi earthquake: influence from inherited fold belt structures: J. Struct. Geol., 173–192.

Loevenbruck, A., R. Cattin, Pichon, X. Le, S. Dominguez, and R. Michel, 2004, Coseismic slip resolution and post-seismic relaxation time of the 1999 Chi-Chi, Taiwan, earthquake as constrained by geological observations, geodetic measurements and seismicity: Geophys. J. Int., **158**, 310–326.

Ma, K., J. Mori, S. Lee, and S. Yu, 2001, Spatial and temporal slip distribution of slip for the 1999 Chi-Chi, Taiwan earthquake: Bull. seism. Soc. Am., **91**, 1069–1087.

Rice, J., 1983, Constitutive relations for fault slip and earthquake instabilities: Pure and applied geophysics, **121**, 443–475.

Segall, P., 2010, Earthquake and volcano deformation.

Sheu, S.-Y. and C.-F. Shieh, 2004, Viscoelasticafterslip concurrence: a possible mechanism in the early post-seismic deformation of the mw 7.6, 1999 Chi-Chi (Taiwan) earthquake: Geophysical Journal International, **159**, 1112–1124.

Thatcher, W., 1983, Nonlinear strain buildup and the earthquake cycle on the San Andreas fault: Geophys. J. Int., **88**, 5893–5902.

Yu, S., 2001, Preseismic deformation and coseismic displacements associated with the 1999 Chi-Chi, Taiwan earthquake: Bull. seism. Soc. Am., **91**, 995–1012.

Yu, S.-B., Y.-J. Hsu, L.-C. Kuo, and H.-Y. Chen, 2003, Gps measurement of postseismic deformation following the 1999 Chi-Chi, Taiwan, earthquake: JOURNAL OF GEOPHYSICAL RESEARCH, **108**, doi:10.1029/2003JB002396.

Zeng, Y. and C. Chen, 2001, Fault rupture process of the 20 september 1999 Chi-Chi, Taiwan, earthquake: Bull. seism. Soc. Am., **91**, 1088–1098.